# Au@Ag Core–Shell Nanocubes for Efficient Plasmonic Light Scattering Effect in Low Bandgap Organic Solar Cells

Se-Woong Baek,[†] Garam Park,[‡] Jonghyeon Noh,[†] Changsoon Cho,[†] Chun-Ho Lee,[§] Min-Kyo Seo,[§] Hyunjoon Song,[‡,*] and Jung-Yong Lee[†,*]

[†]Graduate School of Energy, Environment, Water, and Sustainability (EEWS), Graphene Research Center, Korea Advanced Institute of Science and Technology (KAIST), Daejeon 305-701, Republic of Korea, [‡]Center for Nanomaterials and Chemical Reactions, Institute for Basic Science, and Department of Chemistry, Korea Advanced Institute of Science and Technology (KAIST), Daejeon 305-701, Republic of Korea, and [§]Department of Physics, KI for the NanoCentury, Korea Advanced Institute of Science and Technology (KAIST), Daejeon 305-701, Republic of Korea

ABSTRACT In this report, we propose a metal–metal core–shell nanocube (NC) as an advanced plasmonic material for highly efficient organic solar cells (OSCs). We covered an Au core with a thin Ag shell as *a scattering enhancer* to build Au@Ag NCs, which showed stronger scattering efficiency than Au nanoparticles (AuNPs) throughout the visible range. Highly efficient plasmonic organic solar cells were fabricated by embedding Au@Ag NCs into an anodic buffer layer, poly(3,4-ethylenedioxythiophene):poly(styrenesulfonate) (PEDOT:PSS), and the power conversion efficiency was enhanced to 6.3% from 5.3% in poly[N-9-hepta-decanyl-2,7-carbazole-alt-5,5-(4,7-di-2-thienyl-2,1,3-benzothiadiazole)] (PCDTBT):[6,6]-phenyl C_{71}-butyric acid methyl ester (PC$_{70}$BM) based OSCs and 9.2% from 7.9% in polythieno[3,4-b]thiophene/benzodithiophene (PTB7):PC$_{70}$BM based OSCs. The Au@Ag NC plasmonic PCDTBT:PC$_{70}$BM-based organic solar cells showed 2.2-fold higher external quantum efficiency enhancement compared to AuNPs devices at a wavelength of 450–700 nm due to the amplified plasmonic scattering effect. Finally, we proved the strongly enhanced plasmonic scattering efficiency of Au@Ag NCs embedded in organic solar cells *via* theoretical calculations and detailed optical measurements.
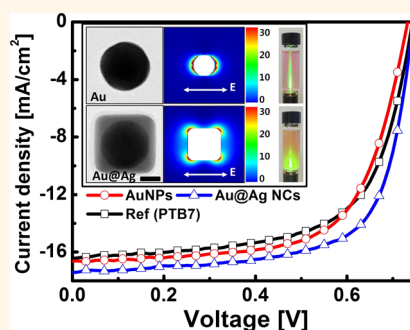
KEYWORDS: plasmonics · forward light scattering · metal nanoparticles · core–shell nanoparticles · organic photovoltaics

Organic solar cell (OSC) has much potential for the realization of the next generation of solar cells because they can be fabricated by roll-to-roll processes and have many potential applications, such as building-integrated photovoltaics (BIPV), semitransparent solar cells, and flexible devices. Recently, low-bandgap photoactive materials have drawn a great deal of attention due to their ability to absorb a wider solar spectrum and achieve higher power conversion efficiency (PCE) ratings.[1–4] However, many low-bandgap photoactive materials still show relatively low levels of external quantum efficiency (EQE) of less than 60%, necessitating effective approaches that can boost the EQE. One of the many interesting approaches to enhance the EQE is the use of the localized surface plasmon resonance (LSPR) effect of metal nanoparticles (MNPs) in devices.

The LSPR effect is a wavelength-dependent optical property of metal nanoparticles. The most attractive aspect of metal nanoparticles is that the optical properties of these particles are controllable by tuning their size, shape and surroundings.[5,6] Therefore, metal nanoparticles have been widely used in many applications, such as photonics,[7] catalysis,[8] chemical and biological sensing[9] and surface-enhanced Raman scattering (SERS).[10] In particular, gold (Au) and silver (Ag) NPs have received attention due to their remarkable LSPR optical properties. Moreover, many researchers have tried to synthesize various types of NPs to improve the performance levels of Au and Ag. Examples include cube,[11]

wire,[12] plate,[13] bimetallic,[14] hollow,[15] and core—shell[16,17] structures.

The LSPR effect of metal nanoparticles has great potential to enhance the absorption of organic solar cells by means of the plasmonic light scattering effect.[18,19] In addition, the tunability of the optical properties of metal nanoparticles offers the possibility that it can be used as an optical engineering tool in organic solar cells.[20] Therefore, many previous reports investigated how plasmonic organic solar cells can enhance the absorption of organic solar cells,[18−36] leading to an EQE enhancement. Notably, AuNPs were commonly used as a plasmonic material in many reports due to their better stability and broader LSPR properties in a longer visible wavelength range than AgNPs.[15,21−23,25−27,30,33,37−39] While seldom discussed, utilizing AuNPs is intrinsically limited due to the low scattering efficiency of AuNPs compared to its level of self-absorption. In contrast, the scattering efficiency of AgNPs is high, although the LSPR region is limited to a wavelength of 400−500 nm, which makes it difficult to manipulate the broad wavelength range using AgNPs, especially at a long wavelength. To overcome this problem, some previous reports[22,30,32,40] mixed various types of metal nanoparticles with organic solar cells to realize a higher absorption enhancement in the visible wavelength range. However, the fundamental problem of metal nanoparticles having a narrow scattering wavelength region or low scattering efficiency was not fully solved.

Therefore, for highly efficient plasmonic organic solar cells, it is necessary to design custom plasmonic metal nanoparticles that have both a broad LSPR region and high scattering efficiency especially at long wavelength range. In this report, we suggest the Au@Ag core—shell nanocube (NC) structure[41,42] to combine the strong scattering power of AgNPs and the broad spectral response of AuNPs at a long wavelength range. We found that a thin Ag shell acted as a strong plasmonic *scattering enhancer* in Au@Ag NCs, solving the above-mentioned problem.

We confirmed that the EQE and absorption of Au@Ag core—shell NC-embedded organic solar cells were improved at a long wavelength significantly compared to AuNP-embedded organic solar cells due to the enhanced plasmonic scattering efficiency. Finally, we showed concrete evidence of the plasmonic scattering effect using near-field optical microscopy (NSOM) and Raman spectroscopy measurements along with analytic optical simulations.

RESULTS AND DISCUSSION

Plasmonic Design of Organic Solar Cells Using AuNPs and AgNPs. The plasmonic organic solar cells device structure is illustrated in Figure 1a. The two types of metal nanoparticles were incorporated into the poly-(3,4-ethylenedioxythiophene):poly(styrenesulfonate) (PEDOT:PSS) layer to induce the plasmonic light scattering effect. A 20 vol % of metal nanoparticles solution was mixed with the PEDOT:PSS solution and spun onto the substrates. Refer to the Methods section for more details. The device structure was glass/ITO/PEDOT:PSS/polymer:PC$_{70}$BM/TiO$_x$/Al. Poly[N-9-heptadecanyl-2,7-carbazole-*alt*-5,5-(4,7-di-2-thienyl-2,1,3-benzothiadiazole)] (PCDTBT), and a polythieno[3,4-*b*]thiophene/benzodithiophene (PTB7) were used as the photoactive polymer donors.

Because the plasmonic properties of metal nanoparticles are wavelength-dependent, a suitable choice of the metal nanoparticles in plasmonic organic solar cells depending on the spectral responses of the active materials is crucial to maximize the benefits of these materials. To show the optical manipulation of metal nanoparticles in organic solar cells, Figure 1b,c shows the EQE and absorption spectra of two types of PCDTBT:PC$_{70}$BM devices. Note that we intentionally changed the thickness and donor/acceptor ratio to modulate the absorption spectra. The detailed modulation methods and characterization of two types of PCDTBT:PC$_{70}$BM devices were described in Methods. The Type I is conventional PCDTBT:PC$_{70}$BM device that has high absorption from 450−600 nm (Figure 1b). However, the absorption of Type II device is low at longer wavelength region, but high at shorter wavelength (<450 nm) (Figure 1c), showing complementary spectral responses to Type I in visible wavelength region. We incorporated 50 nm AgNPs in the Type I device (Figure 1b) and 50 nm AuNPs in the Type II device (Figure 1c). We also optimized the incorporating concentration of the AgNPs and AuNPs, as shown in Supporting Information Figure S1. We reported that a proper incorporating concentration of metal nanoparticles in PEDOT:PSS layer was critical to maximize their full potential without the aggregation of the metal nanoparticles.[43] The current density−voltage (J−V) characteristics and complete device performances at an optimized concentration of AgNPs and AuNPs are depicted in Supporting Information Figure S2 and summarized in Table 1, respectively. The EQE and absorption values were measured to study the wavelength dependency of the optical properties of the metal nanoparticles.

The Type I device shows an absorption dip at a wavelength of 400−500 nm. The low absorption can be significantly improved by AgNPs whose LSPR position perfectly overlaps the region (blue line in Figure 1b), a finding in good agreement with our previous report.[43] On the other hand, the Type II device shows relatively low absorption at a wavelength of 500−650 nm, suggesting that the AuNPs (blue line in Figure 1c) are seemingly more appropriate to enhance the PCE than the AgNPs. Experimentally, the EQE and absorption enhancement regions were well matched with the corresponding LSPR peaks (blue lines in
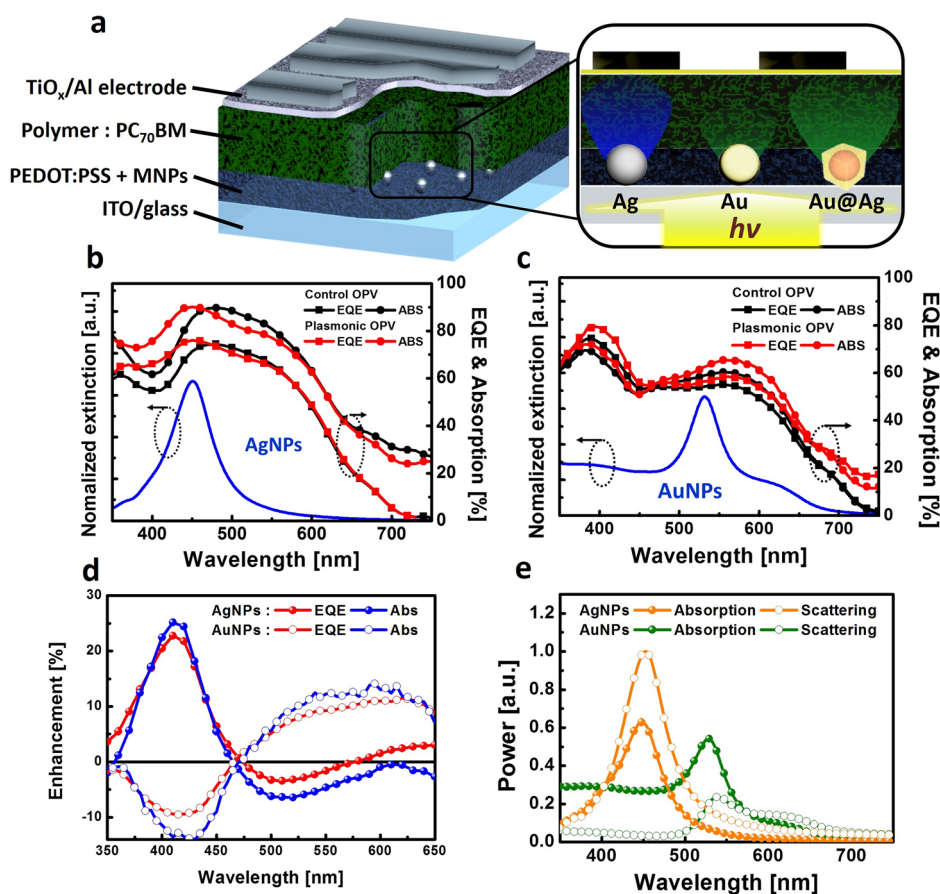
Figure 1. Optical engineering by plasmonic MNPs. (a) Schematic of a plasmonic OSC. The device structure is glass/ITO/PEDOT:PSS with MNPs/PCDTBT:PC$_{70}$BM (or PTB7:PC$_{70}$BM)/TiO$_x$/Al. (b) The EQE (squares) and absorption (circles) of a Type I control device (black) and a plasmonic device fabricated with AgNPs embedded (red). The blue line represents the normalized extinction spectra of 50 nm AgNPs in PEDOT:PSS. (c) The EQE (squares) and absorption (circles) characteristics of a Type II control device (black) and a plasmonic device fabricated with AuNPs embedded (red). The blue line represents the normalized extinction spectra of 50 nm AuNPs in PEDOT:PSS. (d) The EQE (red) and absorption (blue) enhancements of the AgNP-based plasmonic OSC (filled) and the AuNP-based plasmonic OSC (open). (e) The absorption (filled) and scattering (open) power of the 50 nm AuNPs (green) and AgNPs (yellow). The optical simulations were calculated in a PEDOT:PSS medium.

TABLE 1. Characteristics of Plasmonic Devices Incorporating MNPs in a PEDOT:PSS Layer[a]

polymer			V_{oc} [V]	J_{sc} [mA/cm^2]	FF [%]	η [%]
PCDTBT	Type I (Figure 1b)	Control	0.89 ± 0.00 (0.89)	11.22 ± 0.10 (11.23)	0.64 ± 0.02 (0.65)	6.39 (6.50)
		AgNPs	0.89 ± 0.00 (0.89)	12.41 ± 0.10 (12.51)	0.66 ± 0.01 (0.66)	7.29 (7.35)
	Type II (Figures 1c and 3c)	Control	0.87 ± 0.00 (0.87)	10.32 ± 0.10 (10.44)	0.58 ± 0.00 (0.58)	5.21 (5.29)
		AuNPs	0.87 ± 0.01 (0.87)	10.71 ± 0.16 (10.97)	0.63 ± 0.01 (0.63)	5.87 (6.01)
		Au@Ag NCs	0.87 ± 0.01 (0.87)	11.10 ± 0.23 (11.33)	0.63 ± 0.01 (0.64)	6.08 (6.31)
PTB7	(Figure 3c)	Control	0.74 ± 0.00 (0.74)	16.43 ± 0.10 (16.53)	0.64 ± 0.01 (0.65)	7.78 (7.95)
		AuNPs	0.73 ± 0.01 (0.73)	16.64 ± 0.12 (16.74)	0.67 ± 0.01 (0.68)	8.14 (8.31)
		Au@Ag NCs	0.74 ± 0.01 (0.75)	17.38 ± 0.23 (17.50)	0.68 ± 0.02 (0.70)	8.74 (9.19)

[a] The information in parentheses illustrates the best cell performance for each device.

Figure 1b,c), as calculated by analytic optical simulations performed in PEDOT:PSS. The plasmonic forward scattering effect of metal nanoparticles mainly assisted to enhance the absorption of organic solar cells.[43]

As a comparative experiment, AuNPs were incorporated into the Type I device at the optimized concentration shown in Figure S3; the enhancement was low and we could not clearly verify the exact LSPR scattering effect of the AuNPs because the absorption of the control device at a longer wavelength range was already high, as shown in Supporting Information Figure S3b. Therefore, it can be concluded that the proper choice of metal nanoparticles to compensate for the weak absorption region of a device is of prime importance in designing plasmonic organic solar cells.

The Limitation of AuNPs at Long Wavelengths. Figure 1d illustrates the EQE and absorption enhancement of the Type I (AgNPs) and II (AuNPs) organic solar cells. The similarity of the results of the EQE and the absorption enhancement implies that the EQE enhancement was mainly due to the optical gain caused by the metal nanoparticles. In addition, the enhancement regions are in good agreement with the LSPR peaks of the metal nanoparticles. However, the EQE and absorption enhancement of the organic solar cells with the AuNPs incorporated is relatively low compared to the AgNP-embedded devices despite the optimized incorporating concentration. The low EQE and absorption enhancement are due to the lower scattering efficiency of the AuNPs compared to the AgNPs. Figure 1e shows the results of simulations of the optical scattering and absorption power of AgNPs and AuNPs, both 50 nm in size, in PEDOT:PSS. For the AgNPs, the scattering power is greater than the absorption power, while the AuNPs show lower scattering efficiency and strong self-absorption power despite the broadband scattering response at a longer wavelength in the visible range. Therefore, the enhancement factor of the absorption by active materials is limited due to the intrinsically low scattering efficiency of AuNPs. Note that the absorption of device was enhanced even though the parasitic self-absorption is higher than scattering in overall visible wavelength region (Figure 1e). However, if the absorption of a control device is high, the absorption enhancement becomes low because the portion of non-absorbed light is low. In this report, PCDTBT:PC$_{70}$BM (Type II) (Figure 1c) showed higher absorption enhancement in longer wavelength region than PTB7:PC$_{70}$BM (Supporting Information Figure S3) due to the lower absorption of active layer.

Enhancing the scattering efficiency can be readily achieved by increasing the size of the AuNPs.[43] Supporting Information Figure S4a shows that the scattering and absorption power grow with an increase in the size of the metal nanoparticles; the scattering enhancement rate is much faster than the increased absorption rate. Supporting Information Figure S4b depicts the scattering-to-absorption ratio integrated from 300 to 800 nm for AgNPs and AuNPs at various sizes. The rate of increase of the scattering power of the AgNPs and AuNPs exceeds that of the absorption power when

their sizes exceed 40 and 75 nm, respectively. This suggests that enhancing the scattering efficiency of AuNPs by size tuning is not as effective as it is with AgNPs. Furthermore, in thin-film devices with a thickness of a few hundreds nanometers, incorporating metal nanoparticles larger than 100 nm may not be appropriate. As such, manipulation of the optical properties of AuNPs by changing their size is intrinsically limited as an optical engineering tool in organic solar cells. To ensure a high absorption enhancement factor at wavelengths of 500−650 nm, a novel approach is needed other than pure AuNPs.

Designing Au@Ag Core−Shell NCs and Optical Simulations. We suggest a metal−metal core−shell structure[41] to overcome the intrinsically weak scattering efficiency of AuNPs by constructing a hybrid plasmonic structure consisting of both gold and silver. A thin Ag shell covers the Au core to function as *a scattering enhancer*. We designed the core−shell NCs to achieve both a high scattering efficiency of AgNPs and a feasible broadband absorption enhancement of AuNPs, especially at a long wavelength. To study the fundamental plasmonic scattering behavior of core−shell structures in more detail, we initially calculated the total scattering power analytically at wavelengths of 300−800 nm and calculated the LSPR peak blue shift of the core−shell NCs by controlling the shell thickness, as illustrated in Figure 2a. The diameter of the Au core was fixed at 45 nm and the thickness of the Ag shell was varied from 0 to 30 nm. As the shell thickness increased, the scattering power improved significantly while the LSPR peak was slightly blue-shifted. When the Ag shell thickness was thicker than 20 nm, the scattering power and LSPR peaks both approached those of the AgNPs (red region in Figure 2a), suggesting that metal nanoparticles completely lose their core−shell properties. Therefore, it can be concluded that the appropriate shell thickness should be less than 15 nm (blue region in Figure 2a) to minimize the blue shift of the LSPR while maximizing the scattering power of the metal nanoparticles.

Second, we calculated the wavelength-dependent optical enhancement of the newly designed core−shell NCs compared with AuNPs. Figure 2b shows the calculated absorption and scattering power of AuNPs (45 nm) and Au@Ag NCs (45 nm@10 nm) in PEDOT:PSS. Interestingly, the scattering power was significantly enhanced throughout the visible range with only a 10 nm-thick Ag shell. Hence, we expect that the EQE and absorption enhancement of plasmonic organic solar cells can be improved further throughout the visible range centered at ∼520 nm with Au@Ag NCs as opposed to AuNPs.

Synthesis and Characterization of Au@Ag NCs. Figure 2c shows a scanning electron microscope (SEM) image of fully developed Au@Ag NCs. In the inset of Figure 2c, the X-ray diffraction (XRD) results of the AuNPs and
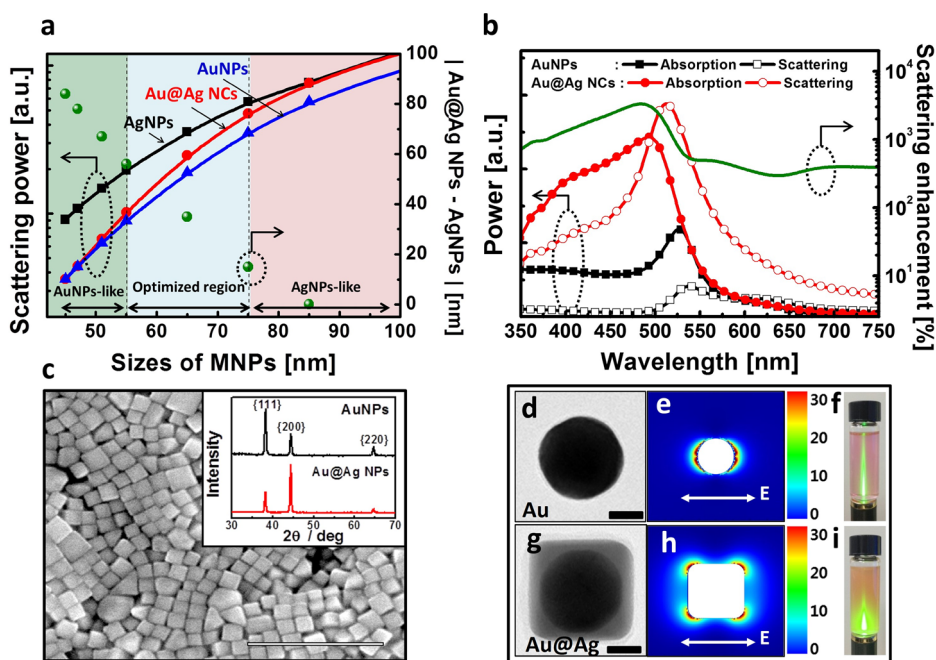
Figure 2. Design and synthesis of Au@Ag NCs. (a) The total scattering power of AgNPs (black squares), AuNPs (blue up triangles), and Au@Ag NCs (red circles). The total scattering power was integrated from 300−800 nm. The difference in the location of the LSPR peak between the AgNPs and the Au@Ag NCs at each size (green circles) is shown. The blue area denotes the appropriate core−shell NCs size region and red area shows the region in which the optical property of the core−shell NCs is completely changed to that of silver. The optical simulations were done in a PEDOT:PSS medium. (b) The scattering power (open) and absorption power (filled) of the 45 nm AuNPs (black squares) and the 45 nm@10 nm Au@Ag NCs (red circles). The scattering enhancement of the Au@Ag NCs compared to that of the AuNPs is plotted as a green line. The optical simulations assumed a PEDOT:PSS medium. (c) SEM image of Au@Ag NCs (scale bar: 500 nm). The inset shows XRD patterns of the AuNPs (black) and Au@Ag NCs (red). (d) TEM image of AuNPs (scale bar: 20 nm). (e) The scattered electric field $|E|^2$ distribution of 45 nm AuNPs. (f) A scattering image of AuNPs. (g) TEM image of Au@Ag NCs (scale bar: 20 nm). (h) The scattered electric field $|E|^2$ distribution of the 45 nm@10 nm Au@Ag NCs. (i) A scattering image of Au@Ag NCs. The scattered electric field $|E|^2$ distribution results (e and h) were calculated at a wavelength of 530 nm using a 3D FDTD method. The medium was assumed to have a constant refractive index ($n = 1.36$), and the total-field scattered-field (TFSF) light source was used with a propagation normal to the image plane and E-field oscillation along the horizontal direction as indicated by an arrow. The MNPs in the scatter images (f and i) were dispersed in an ethanol solution at the same optical density under green laser (532 nm, 1 mW) illumination.

Au@Ag NCs depict facets that dominate the surface as well as the spontaneous orientation of the NPs on the substrate. The spherical AuNPs typical have intensity ratios between the {111}, {200}, and {220} peaks (Au JCPDS 04-0784, Ag JCPDS 04-0783). In contrast, the {200} peak became the most intensive for the Au@Ag NCs, indicating that the alignment of the NPs along the {100} planes that is normal to the substrate due to the perfect cubic morphology. The transmission electron microscopy (TEM) images are single-particle images of AuNPs (Figure 2d) and Au@Ag NCs (Figure 2g), showing that the nanocubes have a dark spherical core at the center. The concentric arrangement of the cubic shell and the spherical core is attributed to the symmetric growth of silver on the gold surface. The average edge length of the Au@Ag NCs was estimated to be 60 ± 6 nm (Supporting Information Figure S5c,d), and the energy dispersive X-ray spectroscopy (EDX) analysis in Supporting Information Figure S6 estimates the elemental fractions of Au and Ag to be 50.8 and 49.2%, respectively. Figure 2e,h depicts the optical scattered field distribution around the AuNPs (45 nm)

and Au@Ag NCs (45 nm@10 nm) at a wavelength of 530 nm employing a 3D finite-difference-time-domain (FDTD) method. These results show that the Au@Ag NCs have a stronger scattered field near the metal nanoparticles surface than the AuNPs, which is in good agreement with the result shown in Figure 2b. Figure 2f,I shows the scattering of AuNPs and Au@Ag NCs dispersed in ethanol at the same optical density when illuminated by a green laser (wavelength: 532 nm). Indeed, the laser is scattered more strongly before it reaches the top in the Au@Ag NC solution than in the AuNPs. The normalized extinction spectra of AuNPs and Au@Ag NCs were depicted in Supporting Information Figure S5e. The original AuNPs have a maximum peak at 526 nm,[41] and the LSPR is slightly shifted to 519 nm in the Au@Ag NCs. The blue shift of the LSPR indicates that the increment of the Ag component altered the effective dielectric constants, making them closer to those of bulk silver.

Photovoltaic Performance. Figure 3a shows the representative J−V characteristics of the control devices (PCDTBT:PC$_{70}$BM (Type II) and PTB7:PC$_{70}$BM) and the
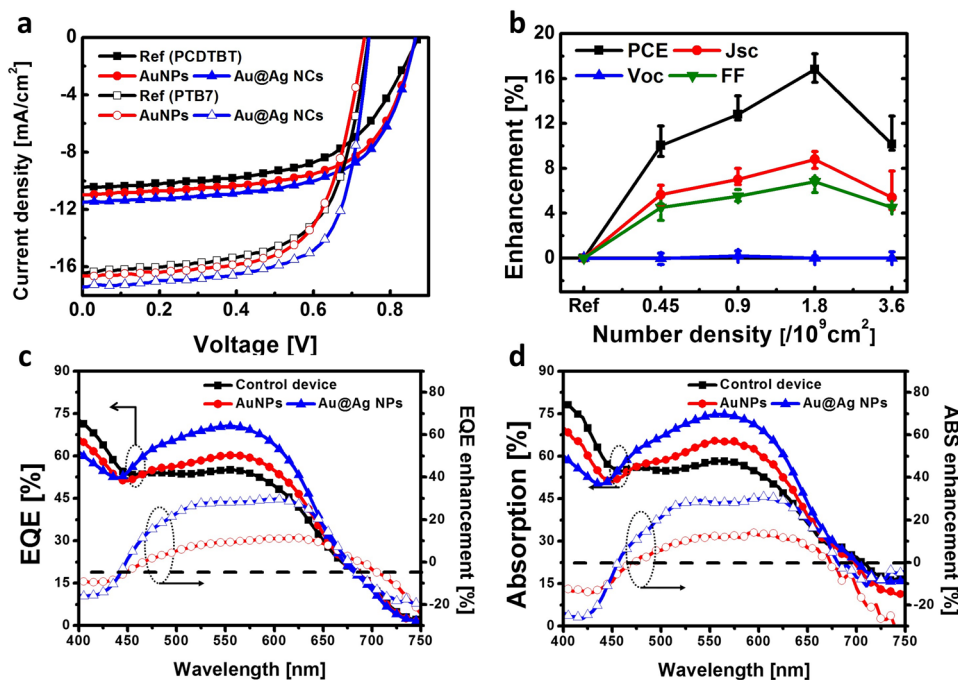
Figure 3. Device characteristics and spectral responses of plasmonic OSCs. (a) Current density−voltage (J−V) characteristics of a control device (black squares) and the best plasmonic OSCs with AuNPs (red circles) and Au@Ag NCs (blue up triangles) embedded. The filled and open symbols denote the PCDTBT:PC$_{70}$BM (Type II) and PTB7:PC$_{70}$BM devices, respectively. **(b)** The PCE (black squares), J_{sc} (red circles), V_{oc} (blue up triangles), and FF (green down triangles) enhancements of the plasmonic OSCs with Au@Ag NCs embedded at various concentrations in a PEDOT:PSS layer. The error bars depict the standard deviation of the performances. The active layer was PCDTBT:PC$_{70}$BM (Type II). **(c)** The EQE (filled symbols) and EQE enhancements (open symbols) of a control device (black squares), AuNP-based OSC (red circles) and Au@Ag NC-based OSC (blue up triangles). The PCDTBT:PC$_{70}$BM (Type II) was used as an active layer. **(d)** The absorption (filled symbols) and absorption enhancements (open symbols) of a control device (black squares), AuNPs-based OSC (red circles) and Au@Ag NCs-based OSC (blue up triangles), where PCDTBT:PC$_{70}$BM (Type II) was used as an active layer.

plasmonic devices under optimized conditions. In this report, we fabricated devices embedding AuNPs and Au@Ag NCs as plasmonic organic solar cells. We chose Au nanoparticle (NP) rather than Au nanocube (NC) because we wanted to show that our new Au@Ag NCs had superior plasmonic scattering property to the conventional AuNPs that many previous reports frequently used. When the AuNPs (45 nm) and Au@Ag NCs (45 nm@10 nm) were incorporated into the PEDOT:PSS layer, both the PCE and J_{sc} values of the plasmonic organic solar cells were enhanced. In particular, the PCE enhancement of an Au@Ag NC-incorporated organic solar cells was superior to that of an AuNP-incorporated device. The average PCE of the PCDTBT:PC$_{70}$BM-based organic solar cells was improved by 16%, from 5.21% to 6.08% and the best performance was 6.31% with 18% PCE enhancement. The PCE of PTB7:PC$_{70}$BM was enhanced by approximately 12%, from 7.78% to 8.74% and the highest PCE was 9.19% with 15% improvement. The complete performances are summarized in Table 1. Figure 3b illustrates the enhancement tendency with increased concentrations of Au@Ag NCs embedded in the anodic buffer layer, revealing that the PCE enhancement mainly results from the J_{sc} and FF (fill factor) enhancement. Specifically, the enhancement of J_{sc} and FF was 8.8% and

6.8%, respectively. Since the FF is related to the electrical properties of the devices, we studied hole mobility and photovoltaics performances (V_{oc} and FF) as a function of light intensity in Supporting Information Figure S7. We found that the charge collection efficiency was enhanced due to the enhanced charge mobility.[37−39] The detailed origin of electrical improvement in plasmonic organic solar cells will be further investigated. As shown in the Table 1, the V_{oc} was mostly unchanged.

To investigate the origin of the J_{sc} and PCE enhancement, we measured the spectral responses of the organic solar cells. Figure 3c shows the EQE and its enhancement in the plasmonic devices incorporating AuNPs and Au@Ag NCs, demonstrating that the EQE was enhanced in nearly the same band from 450− 700 nm upon the embedding of the AuNPs and Au@Ag NCs. It should be noted that the EQE enhancement of the Au@Ag NC-embedded organic solar cells at a wavelength of 450−700 nm is 2.2-fold higher than that of the AuNP-embedded devices. The current density measured by solar simulator and EQE were well-matched within an error range of 3% and summarized in Supporting Information Table S1. Similar trends were confirmed for the absorption and its enhancement, as depicted in Figure 3d. Note that the

IQE of the plasmonic devices was mostly unchanged, as illustrated in Supporting Information Figure S8, implying that the EQE enhancement of both devices is primarily improved by the absorption enhancement. The absorption enhancement in the Au@Ag NC-embedded device was improved by 2.2-fold compared to the AuNP-embedded device at wavelengths of 450−700 nm. It can be inferred that the 10 nm-thick Ag shell helped to enhance the plasmonic scattering power of the Au core significantly with little modulation of the spectral range. As shown in Figure 3d, the absorption was partially degraded at the wavelength of 400−450 nm presumably due to the self-absorption enhancement of the Au@Ag NCs, as expected from the simulation result in Figure 2b. The similar trend was shown in PTB7:PC$_{70}$BM-based plasmonic organic solar cells as illustrated in Supporting Information Figure S9. The EQE and absorption were broadly enhanced from 450−700 nm due to the enhanced plasmonic scattering power of Au@Ag NCs. However, the enhancement of the PTB7:PC$_{70}$BM-based organic solar cells is less pronounced than PCDTBT:PC$_{70}$BM-based organic solar cells because it already has high absorption in overall visible wavelength region.

Many previous reports about plasmonic organic solar cells fully embedded the metal nanoparticles in PEDOT:PSS considering the side effects.[21−23,25,30,31] In this experiments, the morphological effect possibly influences on the device performance because the size of metal nanoparticles (∼ 65 nm) is larger than the thickness of PEDOT:PSS layer (30 nm). The FF enhancement possibly comes from the morphology change of PEDOT:PSS due to the large size of metal nanoparticles. However, based on our previous report,[36] the plasmonic optical effect was dominant compared to the morphological effect (geometrical scattering) in this device configuration. Therefore, in this report, we focused on the plasmonic optical effect of metal nanoparticles in organic solar cells.

Optical Measurements. We systematically investigated the plasmonic scattering effect of the metal nanoparticles in organic solar cells by employing two optical measurement methods: near-field scanning optical microscopy (NSOM) and Raman spectroscopy. Figure 4a illustrates the schematics of the optical measurements. Detailed operations are described in the Methods section.

NSOM Imaging. We visualized the degree of scattering of AuNPs and Au@Ag NCs embedded in a PEDOT:PSS layer using NSOM.[43] We measured the NSOM signal of plasmonic scattering layers consisting of an anodic buffer layer and metal nanoparticles for a full understanding of the origin of the absorption enhancement. The NSOM transmission mode was used, in which the incident light passes through the glass/ITO/PEDOT:PSS with metal nanoparticles and the evanescent wave is captured in the NSOM tip in proximity to the sample surface, as schematically shown in Figure 4a. The incident light was a green laser (wavelength: 532 nm, ∼20 mW), close to the LSPR of the AuNPs and Au@Ag NCs.

Figure 4b−d shows NSOM images of pristine PEDOT:PSS (Figure 4b), PEDOT:PSS with AuNPs (Figure 4c), and PEDOT:PSS with Au@Ag NCs (Figure 4d), and the insets show the scattering profiles along the center lines in the corresponding signal images. When the metal nanoparticles were incorporated into the PEDOT:PSS layer, bright spots were detected and the scattering profile surfaces were rougher than bare PEDOT:PSS. The bright spots represent *hot spots* due to the strong local forward scattering region.[44] The root-mean-square (RMS) values (*i.e.*, the degree of scattering) of the samples were 0.57 (PEDOT:PSS only), 0.71 (AuNPs), and 1.08 (Au@Ag NCs). The enhancement is 24.56% with the AuNPs and 88.94% with the Au@Ag NCs compared to bare PEDOT:PSS film. The scattering enhancement of the Au@Ag NCs is approximately 3-fold higher than that of the AuNPs, agreeing well with the absorption enhancement, as shown in Figure 3d (see also the optical simulation results in Figure 2b). These results clearly prove that the scattering is enhanced further by the improved plasmonic forward scattering effects of Au@Ag NCs.[43]

Raman Spectroscopy. We used Raman spectroscopy to verify that the photons scattered by the metal nanoparticles improve the absorption of photoactive materials. The excitation laser wavelength was 514.5 nm, which was near the LSPR peaks of the AuNPs (526 nm) and Au@Ag NCs (519 nm). Indeed, the Raman intensity was improved when the metal nanoparticles were incorporated in the organic solar cells, as illustrated in Figure 4e. In particular, the Raman intensity of the Au@Ag NCs showed a significant enhancement compared to a control device. The inset of Figure 4e depicts the Raman intensity at 1448 cm^{-1}, which represents the C=C thiophene ring bonding stretch mode of the photoactive materials.[10,25,45] The Raman intensity was increased by 1.5-fold, implying that the plasmonic scattering efficiency of the Au@Ag NCs is superior to that of the AuNPs in terms of enhancing the absorption of the photoactive layer.

In addition, we carried out the 2D Raman imaging of device films to investigate the range of the Raman enhancement induced by the Au@Ag NCs. Figure 4f depicts the integrated Raman intensity value of 1400−1500 cm^{-1} of the device sample (3 μm × 3 μm) with embedded Au@Ag NCs. The bright red spots denote the locally enhanced Raman signal due to the plasmonic scattering effect of the Au@Ag NCs. Figure 4g shows the integrated Raman intensity profiles along the **a** and **b** lines in Figure 4f. The intensity peak of the metal nanoparticles was enhanced by approximately 2-fold compared to that on the spots without metal nanoparticles. We estimated the plasmonic effective cross-section (blue section) in the active layer due to the Au@Ag NCs in Figure 4g. It can be inferred that the plasmonic scattering effect of Au@Ag NCs reaches to 150 nm, covering an area of 70,650 nm^2.
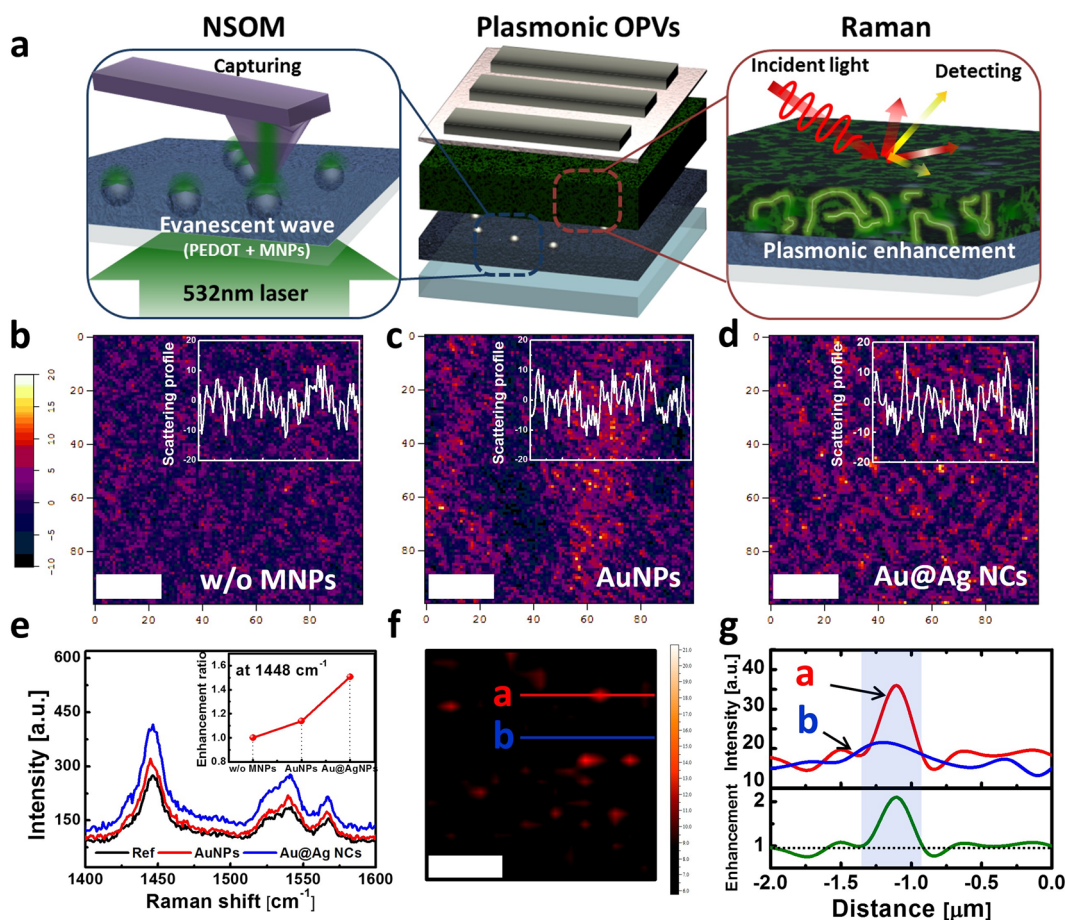
Figure 4. Characterization of plasmonic scattering employing an NSOM and a Raman spectroscopy. (a) The overall schematics of the optical measurements; NSOM images of (b) bare PEDOT:PSS; (c) with AuNPs; (d) with Au@Ag NCs. Scale bars: 1 μm. The samples were prepared under optimized concentrations. The RMS (*i.e.*, degree of scattering) was calculated from the data of each image (5 μm × 5 μm). Insets depict the scattering profile across the center lines of each NSOM image. (e) Raman intensity of the bare PEDOT:PSS (black), AuNPs (red), and Au@Ag NCs (blue). The samples were excited by a 514.5 nm laser. The inset shows the Raman enhancement under each condition at 1448 cm^{-1}. (f) A 2D Raman image of a sample with Au@Ag NCs (3 μm × 3 μm) embedded. The data were integrated from 1400−1500 cm^{-1}. Scale bars: 1 μm. (g) Red and blue lines depict the line profile along lines a and b in panel f, respectively; the green line shows the enhancement factor of the red line. The blue area denotes the plasmonic effective cross-section area in the active layer.

CONCLUSIONS

We demonstrate highly efficient plasmonic organic solar cells with a newly designed embedded Au@Ag core−shell structure. The well-manipulated Au@Ag NCs showed outstanding scattering efficiency at the long wavelength region compared to the AuNPs, while minimizing the blue shift. This suggests that the spectral matching between the LSPR peak of metal nanoparticles and low absorption region of control devices is critical to maximize the EQE and absorption enhancement. The plasmonic PCDTBT:PC$_{70}$BM-based organic solar cells with the embedded Au@Ag NCs showed 2.2-fold absorption enhancement at wavelengths of 450−700 nm compared to AuNPs due to the amplified plasmonic effect of the metal nanoparticles. In addition, a PCE of 9.2% was achieved in PTB7-based organic solar cells. We verified the origin of the PCE enhancement by both theoretical calculations and careful optical measurements. It is also known that the morphology (size and shape) control as well as compositional variation of plasmonic metal nanoparticles largely tune their scattering properties over the full visible ranges. Further efforts to tailor the optical property of metal nanoparticles would be promising to develop high performance organic solar cells. We anticipate that the concepts proposed in this report are not limited to a core−shell structure but can also be used in general plasmonic materials for various optical devices.

METHODS

Synthesis of AgNPs. We synthesized 50 nm AgNPs by a polyol method.[46,47] A 1:20 weight ratio of silver nitrate (AgNO$_3$, 99+ %, Aldrich) and polyvinylpyrrolidone (PVP, M_w: 40 000, Aldrich) was mixed in 20 mL of ethylene glycol (EG) and heated to 140 °C. The reactions were maintained for 4 h and then cooled to room

temperature. The NPs solutions were washed with ethanol at least five times and stored in a refrigerator under a dark condition.

Synthesis of AuNPs. An $AgNO_3$ solution in 1,5-pentanediol (PD, 96%, Aldrich) (0.15 mL, 0.020 M) was added to 25 mL of boiling PD. Then, PVP (M_w = 55 000) (6.0 mL, 0.15 M) and tetrachloroaurate trihydrate ($HAuCl_4\cdot3H_2O$, 99.9+ %, Aldrich) (3.0 mL, 0.05 M) solutions in PD were added every 30 s for 7.5 min. The mixture was then refluxed for 1 h. The product was purified by a repetitive dispersion/precipitation cycle with ethanol and was finally dispersed in 30 mL of ethanol for further reactions.

Synthesis of Au@Ag Core—Shell NCs. The AuNP dispersion in diethylene glycol (DEG, 99%, Aldrich) (1.0 mL, 0.075 M with respect to the gold precursor concentration), PVP (M_w = 55 000, Aldrich) (0.75 mL, 0.30 M), nitric acid (HNO_3, 60−61%, Junsei) (0.0343 mL, 7.5 M), and $AgNO_3$ (0.75 mL, 0.10 M) solutions in DEG was added to DEG (9.0 mL) at 160 °C. The mixture was stirred at that temperature for 1 h. After cooling the mixture, the product was centrifuged and washed three times with deionized water in each case.

Device Fabrication. The devices were fabricated on ITO-coated glass substrates with a sheet resistance of 22 Ω/sq. Glass/ITO substrates were precleaned with a detergent for 25 min, with acetone for 10 min, and with isopropyl alcohol (IPA) for 15 min and then dried in an oven. After an O_2 plasma treatment (90 W, 10 min) on the substrates, both PEDOT:PSS (Al4083, Clevios) layers with and without various metal nanoparticles (20 vol %) were spun onto substrates at 3000 rpm for 30 s and annealed at 140 °C for 10 min. The thickness of the PEDOT layer was approximately 30 nm. PCDTBT:PC_{70}BM (1-materials: Nano-C) at a weight ratio of 1:4 in 1,2-dicholobenzene (o-DCB) solution was completely dissolved for 24 h and then spun at 1100 rpm for 40 s on both PEDOT:PSS layers and then dried at 70 °C for 10 min (Type I). For the Type II of PCDTBT-based device, as shown in Figure 1c, the donor/acceptor ratio was 1:6 and it was spun at 2000 rpm for 40 s. PTB7:PC_{70}BM (1-materials: Nano-C) at a weight ratio of 1:1.5 was dissolved in chlorobenzene:1,8-diiodoctane (97:3) and spun at 2100 rpm for 30 s. The detailed comparison of spectral responses and thickness characterizations of Type I and Type II devices are described in Supporting Information Figure S10. The TiO_x 1:200 solution, dissolved in methanol, was spun at 3000 rpm and dried at 80 °C for 10 min in air. Finally, 150 nm of Al was deposited through a shadow mask by thermal evaporation on the devices. The active device area was measured with a microscope, showing that it was ~15 mm^2. When the metal nanoparticles solution was used without any purification processes such as centrifugation and filtering, remaining reagents and surfactants may influence on the device performance. However, we found that the surfactant (PVP) and other chemical reagents did not affect the device performance. Refer to the Supporting Information.

Characterization. Current density−voltage ($J-V$) characteristics were measured by a solar simulator (PEC-L12, Peccell Technologies) under 100 mW/cm^2 from a 150 W Xe short-arc lamp filtered by an AM 1.5G filter. The external quantum efficiency (EQE) was measured by a spectral measurement system (K3100 IQX, McScience, Inc.). The light source (Xenon arc lamp 300 W) was used with a monochromator (Newport) and an optical chopper (MC 2000 Thorlabs). The spectral absorption by the devices was directly measured at the same spot immediately after the EQE measurement. It should be noted that the measured absorption implies the total absorption including not only the absorption of the active materials but also parasitic absorption sources such as the electrode and PEDOT:PSS. Finally, the internal quantum efficiency (IQE) was determined by dividing the EQE by the absorption. The extinction spectra were measured by UV−vis-NIR spectrophotometers (UV-3600, Shimadzu, and V670 UV−vis-NIR, Jasco). We used unpolarized light in all experiments. For the optical simulations using the FDTD, the mesh size was fixed to 1 nm and the refractive indices of gold and silver were obtained from literature.[48]

To visualize the metal nanoparticles, field emission scanning electron microscopy (FE-SEM, FEI Sirion, and XL30S FEG, Philips) was used. X-ray diffraction (XRD) patterns were recorded on a Rigaku D/max-IIIC (3 kW) diffractometer using Cu Kα radiation.

Silicon wafers (P-100) were used for the SEM and XRD measurements. The field emission transmission electron microscope (FE-TEM, FEI Tecnai G^2 f30 S-Twin, 300 KeV) and (FE-TEM, JEOL FB-2100F HR, 200 kV) were used to investigate the detail structure of metal nanoparticles. Energy dispersive X-ray spectroscopy (EDX, FEI Sirion) spectra was used to characterize the elements of the AuNPs and Au@Ag NCs.

Near-Field Scanning Optical Microscopy. A scanning near-field optical microscope (Alpha300S, WiTec) was used to measure the NSOM signal (*i.e.*, the scattering profile). To scan the NSOM signal images, the incident light source was a green light laser (wavelength: 532 nm), which excited the PEDOT:PSS film with metal nanoparticles near the LSPR wavelength, and the aperture size was 60 nm. The detailed NSOM measurement process followed that of a previous report.[43] In short, the NSOM tip captures the evanescent wave while scanning the samples above the PEDOT:PSS surface. Then, signals are collected and converted to profile images. The scattering profiles (Figure 4b−d, insets) were surface line graphs of the NSOM signal images. The NSOM signals were scanned in an area of 5 μm × 5 μm. The scanning rate was 1 s/line.

Raman Spectroscopy. A high-resolution dispersive Raman microscope (ARAMIS, Horiba Jobin Yvon) was used to measure the Raman intensity (Figure 4e). It was also used for Raman imaging (Figure 4f). An Ar^+ ion CW laser (wavelength: 514.5 nm) was used as an excitation source up to 40 mW for each sample. The measurement data was acquired at room temperature. In the case of Raman imaging, we scanned the film under the same conditions shown in Figure 4e. The laser spot was about 500 nm and the scanning spacing was 200 nm. The Raman images were acquired by scanning an area of 3 μm × 3 μm. We used Labspec5 as an image-processing tool. The sample preparation process was identical to the device fabrication process described above. The sample structure was glass/ITO/PEDOT:PSS with a metal nanoparticles/PCDTBT:PC_{70}BM layer. However, the active layer was thinner than the actual device conditions. The active layer solution was spun at 5000 rpm for 30 s and dried at 70 °C for 10 min. A TiO_x layer and an Al electrode were not deposited.

Conflict of Interest: The authors declare no competing financial interest.

Supporting Information Available: The detailed performances of AuNPs and AgNPs at various concentrations, $J-V$ characteristics, QE and absorption spectra, optical simulation result of AuNPs, SEM, EDX and size-distribution histogram of AuNPs and Au@Ag NCs, IQE performance and table. This material is available free of charge *via* the Internet at http://pubs.acs.org.

REFERENCES AND NOTES

1. Dou, L. T.; Chang, W. H.; Gao, J.; Chen, C. C.; You, J. B.; Yang, Y. A Selenium-Substituted Low-Bandgap Polymer with Versatile Photovoltaic Applications. *Adv. Mater.* **2013**, *25*, 825−831.

2. You, J. B.; Dou, L. T.; Yoshimura, K.; Kato, T.; Ohya, K.; Moriarty, T.; Emery, K.; Chen, C. C.; Gao, J.; Li, G.; *et al.* A Polymer Tandem Solar Cell with 10.6% Power Conversion Efficiency. *Nat. Commun.* **2013**, *4*, 1446.

3. Liang, Y. Y.; Xu, Z.; Xia, J. B.; Tsai, S. T.; Wu, Y.; Li, G.; Ray, C.; Yu, L. P. For the Bright Future-Bulk Heterojunction Polymer

Solar Cells with Power Conversion Efficiency of 7.4%. *Adv. Mater.* **2010**, *22*, E135–E138.

4. Sun, Y. M.; Welch, G. C.; Leong, W. L.; Takacs, C. J.; Bazan, G. C.; Heeger, A. J. Solution-Processed Small-Molecule Solar Cells with 6.7% Efficiency. *Nat. Mater.* **2012**, *11*, 44–48.

5. Kelly, K. L.; Coronado, E.; Zhao, L. L.; Schatz, G. C. The Optical Properties of Metal Nanoparticles: The Influence of Size, Shape, and Dielectric Environment. *J. Phys. Chem. B* **2003**, *107*, 668–677.

6. Lu, X. M.; Rycenga, M.; Skrabalak, S. E.; Wiley, B.; Xia, Y. N. Chemical Synthesis of Novel Plasmonic Nanoparticles. *Annu. Rev. Phys. Chem.* **2009**, *60*, 167–192.

7. Green, M. A.; Pillai, S. Harnessing Plasmonics for Solar Cells. *Nat. Photonics* **2012**, *6*, 130–132.

8. Crooks, R. M.; Zhao, M. Q.; Sun, L.; Chechik, V.; Yeung, L. K. Dendrimer-Encapsulated Metal Nanoparticles: Synthesis, Characterization, and Applications to Catalysis. *Acc. Chem. Res.* **2001**, *34*, 181–190.

9. Lee, K. S.; El-Sayed, M. A. Gold and Silver Nanoparticles in Sensing and Imaging: Sensitivity of Plasmon Response to Size, Shape, and Metal Composition. *J. Phys. Chem. B* **2006**, *110*, 19220–19225.

10. Stavytska-Barba, M.; Salvador, M.; Kulkarni, A.; Ginger, D. S.; Kelley, A. M. Plasmonic Enhancement of Raman Scattering from the Organic Solar Cell Material P3HT/PCBM by Triangular Silver Nanoprisms. *J. Phys. Chem. C* **2011**, *115*, 20788–20794.

11. Rycenga, M.; Cobley, C. M.; Zeng, J.; Li, W. Y.; Moran, C. H.; Zhang, Q.; Qin, D.; Xia, Y. N. Controlling the Synthesis and Assembly of Silver Nanostructures for Plasmonic Applications. *Chem. Rev.* **2011**, *111*, 3669–3712.

12. Sun, Y. G.; Mayers, B.; Herricks, T.; Xia, Y. N. Polyol Synthesis of Uniform Silver Nanowires: A Plausible Growth Mechanism and the Supporting Evidence. *Nano Lett.* **2003**, *3*, 955–960.

13. Jin, R. C.; Cao, Y. W.; Mirkin, C. A.; Kelly, K. L.; Schatz, G. C.; Zheng, J. G. Photoinduced Conversion of Silver Nanospheres to Nanoprisms. *Science* **2001**, *294*, 1901–1903.

14. Chen, D. H.; Chen, C. J. Formation and Characterization of Au-Ag Bimetallic Nanoparticles in Water-in-Oil Microemulsions. *J. Mater. Chem.* **2002**, *12*, 1557–1562.

15. Ma, Y. Y.; Li, W. Y.; Cho, E. C.; Li, Z. Y.; Yu, T. K.; Zeng, J.; Xie, Z. X.; Xia, Y. N. Au@Ag Core-Shell Nanocubes with Finely Tuned and Well-Controlled Sizes, Shell Thicknesses, and Optical Properties. *ACS Nano* **2010**, *4*, 6725–6734.

16. Park, G.; Lee, C.; Seo, D.; Song, H. Full-Color Tuning of Surface Plasmon Resonance by Compositional Variation of Au@Ag Core-Shell Nanocubes with Sulfides. *Langmuir* **2012**, *28*, 9003–9009.

17. Shankar, S. S.; Rai, A.; Ahmad, A.; Sastry, M. Rapid Synthesis of Au, Ag, and Bimetallic Au Core-Ag shell Nanoparticles using Neem (*Azadirachta indica*) Leaf Broth. *J. Colloid Interface Sci.* **2004**, *275*, 496–502.

18. Lee, J. Y.; Peumans, P. The Origin of Enhanced Optical Absorption in Solar Cells with Metal Nanoparticles Embedded in the Active Layer. *Opt. Express* **2010**, *18*, 10078–10087.

19. Atwater, H. A.; Polman, A. Plasmonics for Improved Photovoltaic Devices. *Nat. Mater.* **2010**, *9*, 205–213.

20. Jankovic, V.; Yang, Y.; You, J. B.; Dou, L. T.; Liu, Y. S.; Cheung, P.; Chang, J. P. Active Layer-Incorporated, Spectrally Tuned Au/SiO$_2$ Core/Shell Nanorod-Based Light Trapping for Organic Photovoltaics. *ACS Nano* **2013**, *7*, 3815–3822.

21. Li, X. H.; Choy, W. C. H.; Huo, L. J.; Xie, F. X.; Sha, W. E. I.; Ding, B. F.; Guo, X.; Li, Y. F.; Hou, J. H.; You, J. B; *et al.* Dual Plasmonic Nanostructures for High Performance Inverted Organic Solar Cells. *Adv. Mater.* **2012**, *24*, 3046–3052.

22. Chen, H. C.; Chou, S. W.; Tseng, W. H.; Chen, I. W. P.; Liu, C. C.; Liu, C.; Liu, C. L.; Chen, C. H.; Wu, C. I.; Chou, P. T. Large AuAg Alloy Nanoparticles Synthesized in Organic Media Using a One-Pot Reaction: Their Applications for High-Performance Bulk Heterojunction Solar Cells. *Adv. Funct. Mater.* **2012**, *22*, 3975–3984.

23. Xie, F. X.; Choy, W. C. H.; Wang, C. C. D.; Sha, W. E. I.; Fung, D. D. S. Improving the Efficiency of Polymer Solar Cells by Incorporating Gold Nanoparticles into All Polymer Layers. *Appl. Phys. Lett.* **2011**, *99*, 153304.

24. Wang, D. H.; Park, K. H.; Seo, J. H.; Seifter, J.; Jeon, J. H.; Kim, J. K.; Park, J. H.; Park, O. O.; Heeger, A. J. Enhanced Power Conversion Efficiency in PCDTBT/PC(70)BM Bulk Heterojunction Photovoltaic Devices with Embedded Silver Nanoparticle Clusters. *Adv. Energy Mater.* **2011**, *1*, 766–770.

25. Yang, J.; You, J. B.; Chen, C. C.; Hsu, W. C.; Tan, H. R.; Zhang, X. W.; Hong, Z. R.; Yang, Y. Plasmonic Polymer Tandem Solar Cell. *ACS Nano* **2011**, *5*, 6210–6217.

26. Wu, J. L.; Chen, F. C.; Hsiao, Y. S.; Chien, F. C.; Chen, P. L.; Kuo, C. H.; Huang, M. H.; Hsu, C. S. Surface Plasmonic Effects of Metallic Nanoparticles on the Performance of Polymer Bulk Heterojunction Solar Cells. *ACS Nano* **2011**, *5*, 959–967.

27. Kim, K.; Carroll, D. L. Roles of Au and Ag Nanoparticles in Efficiency Enhancement of poly(3-octylthiophene)/C-60 Bulk Heterojunction Photovoltaic Devices. *Appl. Phys. Lett.* **2005**, *87*, 203113.

28. Kulkarni, A. P.; Noone, K. M.; Munechika, K.; Guyer, S. R.; Ginger, D. S. Plasmon-Enhanced Charge Carrier Generation in Organic Photovoltaic Films Using Silver Nanoprisms. *Nano Lett.* **2010**, *10*, 1501–1505.

29. Qu, D.; Liu, F.; Huang, Y. D.; Xie, W. L.; Xu, Q. Mechanism of Optical Absorption Enhancement in Thin Film Organic Solar Cells with Plasmonic Metal Nanoparticles. *Opt. Express* **2011**, *19*, 24795–24803.

30. Lu, L. Y.; Luo, Z. Q.; Xu, T.; Yu, L. P. Cooperative Plasmonic Effect of Ag and Au Nanoparticles on Enhancing Performance of Polymer Solar Cells. *Nano Lett.* **2013**, *13*, 59–64.

31. Silvert, P. Y.; HerreraUrbina, R.; TekaiaElhsissen, K. Preparation of Colloidal Silver Dispersions by the Polyol Process 0.2. Mechanism of Particle Formation. *J. Mater. Chem.* **1997**, *7*, 293–299.

32. Li, X. H.; Choy, W. C. H.; Lu, H. F.; Sha, W. E. I.; Ho, A. H. P. Efficiency Enhancement of Organic Solar Cells by Using Shape-Dependent Broadband Plasmonic Absorption in Metallic Nanoparticles. *Adv. Funct. Mater.* **2013**, *23*, 2728–2735.

33. Yang, X.; Chueh, C. C.; Li, C. Z.; Yip, H. L.; Yin, P. P.; Chen, H. Z.; Chen, W. C.; Jen, A. K. Y. High-Efficiency Polymer Solar Cells Achieved by Doping Plasmonic Metallic Nanoparticles into Dual Charge Selecting Interfacial Layers to Enhance Light Trapping. *Adv. Energy Mater.* **2013**, *3*, 666–673.

34. Choi, H.; Lee, J. P.; Ko, S. J.; Jung, J. W.; Park, H.; Yoo, S.; Park, O.; Jeong, J. R.; Park, S.; Kim, J. Y. Multipositional Silica-Coated Silver Nanoparticles for High-Performance Polymer Solar Cells. *Nano Lett.* **2013**, *13*, 2204–2208.

35. Wang, D. H.; Kim, D. Y.; Choi, K. W.; Seo, J. H.; Im, S. H.; Park, J. H.; Park, O. O.; Heeger, A. J. Enhancement of Donor-Acceptor Polymer Bulk Heterojunction Solar Cell Power Conversion Efficiencies by Addition of Au Nanoparticles. *Angew. Chem., Int. Ed.* **2011**, *50*, 5519–5523.

36. Gan, Q. Q.; Bartoli, F. J.; Kafafi, Z. H. Plasmonic-Enhanced Organic Photovoltaics: Breaking the 10% Efficiency Barrier. *Adv. Mater.* **2013**, *25*, 2385–2396.

37. Pegg, L. J.; Schumann, S.; Hatton, R. A. Enhancing the Open-Circuit Voltage of Molecular Photovoltaics Using Oxidized Au Nanocrystals. *ACS Nano* **2010**, *4*, 5671–5678.

38. Xie, F. X.; Choy, W. C. H.; Sha, W. E. I.; Zhang, D.; Zhang, S. Q.; Li, X. C.; Leung, C. W.; Hou, J. H. Enhanced Charge Extraction in Organic Solar Cells through Electron Accumulation Effects Induced by Metal Nanoparticles. *Energy Environ. Sci.* **2013**, *6*, 3372–3379.

39. Zhang, D.; Choy, W. C. H.; Xie, F. X.; Sha, W. E. I.; Li, X. C.; Ding, B. F.; Zhang, K.; Huang, F.; Cao, Y. Plasmonic Electrically Functionalized TiO2 for High-Performance Organic Solar Cells. *Adv. Funct. Mater.* **2013**, *23*, 4255–4261.

40. Heo, M.; Cho, H.; Jung, J. W.; Jeong, J. R.; Park, S.; Kim, J. Y. High-Performance Organic Optoelectronic Devices Enhanced by Surface Plasmon Resonance. *Adv. Mater.* **2011**, *23*, 5689–5693.

41. Park, G.; Seo, D.; Jung, J.; Ryu, S.; Song, H. Shape Evolution and Gram-Scale Synthesis of Gold@Silver Core-Shell Nanopolyhedrons. *J. Phys. Chem. C* **2011**, *115*, 9417–9423.

42. Seo, D.; Park, J. C.; Song, H. Polyhedral Gold Nanocrystals with O_h Symmetry: From Octahedra to Cubes. *J. Am. Chem. Soc.* **2006**, *128*, 14863–14870.

43. Baek, S. W.; Noh, J.; Lee, C. H.; Kim, B.; Seo, M. K.; Lee, J. Y. Plasmonic Forward Scattering Effect in Organic Solar Cells: A Powerful Optical Engineering Method. *Sci. Rep.* **2013**, *3*, 1726.

44. Talley, C. E.; Jackson, J. B.; Oubre, C.; Grady, N. K.; Hollars, C. W.; Lane, S. M.; Huser, T. R.; Nordlander, P.; Halas, N. J. Surface-Enhanced Raman Scattering from Individual Au Nanoparticles and Nanoparticle Dimer Substrates. *Nano Lett.* **2005**, *5*, 1569–1574.

45. Campoy-Quiles, M.; Ferenczi, T.; Agostinelli, T.; Etchegoin, P. G.; Kim, Y.; Anthopoulos, T. D.; Stavrinou, P. N.; Bradley, D. D. C.; Nelson, J. Morphology Evolution *via* Self-Organization and Lateral and Vertical Diffusion in Polymer: Fullerene Solar Cell Blends. *Nat. Mater.* **2008**, *7*, 158–164.

46. Silvert, P. Y.; HerreraUrbina, R.; Duvauchelle, N.; Vijayakrishnan, V.; Elhsissen, K. T. Preparation of Colloidal Silver Dispersions by the Polyol Process 0.1. Synthesis and Characterization. *J. Mater. Chem.* **1996**, *6*, 573–577.

47. Zhao, T.; Sun, R.; Yu, S. H.; Zhang, Z. J.; Zhou, L. M.; Huang, H. T.; Du, R. X. Size-Controlled Preparation of Silver Nanoparticles by a Modified Polyol Method. *Colloids Surf., A* **2010**, *366*, 197–202.

48. Palik, E. D.; Ghosh, G. *Handbook of Optical Constants of Solids*; Academic Press: San Diego, CA, 1998.